Hierarchical zeolites for dimethyl ether dehydration into light olefins

Catalysis Today 463 (2026) 115618

Contents lists available at ScienceDirect

Catalysis Today

journal homepage: www.elsevier.com/locate/cattod

Hierarchical zeolites for dimethyl ether dehydration into light olefins

Fabio Salomone [a], Giorgia Ferrarelli [b], Emanuele Giglio [b,*], Elena Corrao [c], Massimo Migliori [b], Samir Bensaid [a], Raffaele Pirone [a], Girolamo Giordano [b]

[a] Department of Applied Science and Technology (DISAT), Polytechnic of Turin, Corso Duca degli Abruzzi 24, Turin 10129, Italy
[b] Chemical Engineering and Catalysis for Sustainable Processes (CECaSP) Laboratory, University of Calabria, Via Pietro Bucci, Rende 87036, Italy
[c] Department of Chemistry and NIS Centre, University of Torino, Via Pietro Giuria 7, Turin 10125, Italy

ARTICLE INFO

Keywords:
Hierarchical zeolites
DTO
Light olefins
Deactivation
Kinetics

ABSTRACT

Dimethyl ether (DME) conversion into light olefins (DTO) is a process that can lead to the sustainable production of molecules like ethylene, propylene, and butenes, which are key building blocks in the chemical industry. Acid catalysts involved in the conversion of methanol and DME into hydrocarbons (MTO and DTO) are usually affected by fast deactivation due to coke generation. In the present study, four hierarchical zeolites were synthesized with different Si/Al ratios according to two procedures: a post-treatment (named "etching") of a HZSM-5 microporous zeolite with a solution of ammonium fluoride and hydrofluoric acid, and a one-pot bottom-down approach involving an organosilane to induce mesoporosity during the hydrothermal synthesis. The samples were characterized from a physico-chemical standpoint to assess crystallinity, textural properties, and acidity. All the synthesized zeolites were then tested for about 14 h in the DTO process at a temperature range of 300–375 °C. Results showed that hierarchical zeolites with mild acidity have a very good stability, even when they are tested at the highest temperature, at which conventional microporous samples deactivate quickly. Conversion of 80–90 % is achieved at 375 °C and a space velocity of 1 g_{cat}•h•mol_C^{-1}, with propylene as the most abundant product. Samples prepared via one-pot synthesis resulted in a greater propylene-to-ethylene ratio, partly due to shape selectivity related to the pore size distribution.

1. Introduction

The urgency to mitigate climate change and reduce dependence on fossil resources has driven the development of catalytic processes to produce sustainable fuels and chemicals [1,2]. In this framework, methanol (CH_3OH or MeOH) and dimethyl ether (DME) have emerged as versatile platform molecules for the synthesis of value-added products [3–5]. These molecules can act as energy carriers or fuels in a broad spectrum of applications [6–8]. In addition, MeOH and DME can be used as intermediates in the production of light olefins.

Light olefins are unsaturated hydrocarbons with a carbon-carbon double bond, including ethylene (C_2H_4), propylene (C_3H_6), and butenes (C_4H_8). Light olefins are key building blocks in the petrochemical industry and are involved in various uses and production processes. Most of the ethylene is used to produce low- or high-density polyethylene (PE), polystyrene (PS), polyvinyl chloride (PVC), polyethylene terephthalate (PET), ethylene oxide, ethylene dichloride, ethylbenzene, acetaldehyde, and vinyl acetate [9]. Propene is involved in the manufacturing of polypropylene (PP), acrylonitrile, propylene oxide, propanol, cumene, and acrylic acid [10]. The largest utilization for butenes is the conversion into alkylate species, methyl tert-butyl ether (MTBE), synthetic rubbers, and butadiene [11]. Global yearly production volume in 2023 was equal to 229 Mt and 160 Mt for ethylene and propylene, respectively [12,13], and the forecasted compound annual growth rate (CAGR) is about 4 % for both platform molecules [14,15].

Industrial production of light olefins mainly exploits fossil-based feedstocks via steam cracking, fluid catalytic cracking (FCC), and paraffin dehydrogenation [16]. Most of the light olefins are generally produced via steam cracking by using naphtha (ethane in some cases) as feedstock of a furnace operating in the range 800–900 °C. This process is strongly endothermic and energy-intensive, and the product gas is characterized by a low propylene-to-ethylene (P/E) ratio. Catalytic cracking instead employs a solid catalyst to convert long-chain hydrocarbons, heavy oils, and residues into gasoline-cut and olefins as co-products. The presence of a catalyst reduces the operating temperature (ranging between 485 and 550 ℃) and enables the possibility of

* Corresponding author.
E-mail address: emanuele.giglio@unical.it (E. Giglio).

https://doi.org/10.1016/j.cattod.2025.115618
Received 30 June 2025; Received in revised form 11 October 2025; Accepted 25 October 2025
Available online 27 October 2025

tuning the selectivity of products. The milder temperature allows controlling the P/E ratio to obtain a value above 0.6 [16].

The growing need for de-fossilizing industrial production has driven the development of methanol-to-olefins (MTO) and dimethyl ether-to-olefins (DTO) technologies that convert methanol or DME over an acid catalyst [17–20]. Green methanol could be produced through Power-to-X [21–23] processes using captured CO_2 and renewable H_2 [24]. DME production requires an additional catalytic dehydration step that can also be carried out in the same reactor, leading to a one-pot synthesis [25–27]. If the reacting hydrogen is generated via electrolysis by exploiting renewable energy sources (RES), sustainable production of intermediate molecules and final products (i.e., light olefins) occurs.

MTO and DTO are usually carried out in the temperature range 325–400 °C. The MeOH-DME (de)hydration reaction is considered the first step during MTO/DTO, as it easily occurs over acid zeolites below 300 °C [18,28]. MeOH and DME undergo similar reaction pathways, usually described by the dual cycle hydrocarbon pool concept in the presence of a zeolite or zeotype (such as SAPO-34) acid catalyst [29–31]. According to this mechanism, two linked cycles (alkene and aromatic ones) occur in parallel, leading to the formation of different hydrocarbons. Besides light olefins or paraffins, heavier molecules are generated, like poly-substituted aromatic hydrocarbons. These molecules are commonly considered as coke precursors, leading to the formation of large molecules that may clog the zeolite pores, progressively deactivating the catalyst. The DTO route offers some advantages over the MTO pathway, like faster reaction rates, reduced water formation, and lower exothermicity, which may result in improved catalyst longevity and selectivity towards light olefins [32,33].

As mentioned earlier, zeolites are widely employed as heterogeneous solid acid catalysts in these processes due to their unique combination of Brønsted acidity and shape selectivity [19,34]. Owing to their extensive application in MTO processes, SAPO materials have also been explored for the DTO route [35]. Nevertheless, SAPO-34 suffers from fast deactivation in both processes, primarily due to coke deposition within its microporous framework. To overcome this drawback, hierarchical structures have been synthesized, and the effect of induced mesoporosity was in the direction of improving the catalyst stability [36]. Nanocrystals, instead, facilitate the diffusion of lighter products before they can undergo further conversion into coke [37]. In addition, SAPO catalysts generally show faster deactivation and a lower P/E ratio than other zeolites/zeotypes in the DTO process [38,39].

Therefore, MFI-type zeolites have also been investigated for DTO, with particular emphasis on the role of the Si/Al ratio, and thus the acidity, on sample activity and stability [40]. Most of the published works focused on commercial H-ZSM-5 catalysts formulated with binders [41–43]. Moreover, to describe the complex reaction network and deactivation pathways, lumped kinetic models have been proposed [33,44]. Even for this structure, hierarchical ZSM-5 samples have presented higher stability and a greater P/E ratio [45]. ZSM-5 samples thus stand out due to their versatile MFI topology, tunable acidity through Si/Al ratio control, and excellent hydrothermal stability [45–47]. Its three-dimensional topology of 10-membered ring (MR) channels allows the formation and diffusion of hydrocarbon intermediates, making it a promising candidate for the selective production of light olefins, aromatics, and gasoline-range hydrocarbons [48–51].

However, like any microporous crystal, conventional microporous ZSM-5 suffers from mass transport limitations, particularly in the case of reactions involving bulky intermediates or coke-forming precursors, as the pore size can hinder the diffusion of reactants and products, leading to the accumulation of heavy species and subsequent catalyst deactivation [52]. To address these issues, integrating both mesoporous and macroporous domains into the microporous crystalline framework, the use of hierarchical zeolites has emerged as a promising strategy for catalyst improvement. The incorporation of larger pores improves accessibility to active sites, facilitates the removal of coke precursors, and reduces diffusion path lengths. As a result, hierarchical zeolites typically exhibit enhanced catalytic performance, improved selectivity, and prolonged stability under severe reaction conditions [53]. These advantages are relevant in both MTO and DTO reactions, where rapid removal of reactive intermediates can prevent secondary reactions such as oligomerization and aromatization [54].

Hierarchical porosity in zeolites can be introduced following two primary approaches: (i) top-down methods, such as post-synthesis desilication or acid/base etching of preformed zeolites, and (ii) bottom-up methods, where the mesoporosity is built during the synthesis using templating agents such as surfactants, polymers, or organosilanes [55]. While both strategies can generate hierarchical structures, they may result in different levels of crystallinity, mesopore connectivity, and defect concentration. Therefore, the method of mesopore creation may affect the final acidity profile, framework stability, and overall catalytic behavior of the material [56,57].

In our previous paper, four ZSM-5 samples having different Si/Al ratios (25 or 50) with or without superficial passivation with a Silicalite-1 layer have been synthesized, characterized, and tested for DTO to assess activity, stability, and product distribution. Samples with higher acidity presented higher initial conversion, but lower stability over time [58].

In this work, four hierarchical zeolites with different acidity were prepared according to two different synthesis approaches. The first material was obtained by direct synthesis using an organosilane as an additive, resulting in a bottom-up hierarchical structure [59–61]. The second was derived from a 'parent' ZSM-5, which is treated with a solution of hydrofluoric acid and ammonium fluoride ("etching" procedure), following a top-down approach. For the same zeolite topology, by following two different hierarchization routes, this study aims to elucidate how the nature of mesopore formation impacts the textural, acidic, and catalytic properties of MFI-type zeolite in DTO. Apart from the importance of exploring the catalyst potential for DTO process scale-up, the proposed study also uses a model reaction scheme for studying the interplay between pore architecture and catalyst performance in acid-catalyzed processes. A deeper understanding of these structure–function relationships is critical for guiding the rational design of next-generation zeolite-based catalysts tailored for renewable feedstocks and sustainable chemical manufacturing.

2. Materials and methods

2.1. Synthesis of the catalysts

MFI-type zeolites with Si/Al ratios of 25 and 50 were synthesized following a procedure reported elsewhere [62], and subsequently subjected to a post-synthetic chemical etching treatment. Parent ZSM-5 zeolites in the as-synthesized form (0.5 g) were treated with a fluoride solution consisting of a mixture of NH_4F and HF [63]. Specifically, 2.5 g of NH_4F were dissolved in 15 mL of a 0.5 mol L^{-1} aqueous HF solution, and the zeolite was then dispersed in the resulting buffer solution. The suspension was stirred at room temperature for 6 min. After the treatment, the solid was thoroughly washed with distilled water (to remove residual fluoride species) and dried. The etched material was then obtained in acidic form by primary calcination under nitrogen flow at 550 °C for 8 h (5 °C/min), removing the organic template, followed by double ion exchange with an NH_4Cl solution and a second calcination at the same temperature. The etching procedure was carried out on zeolites whose pores still contained the organic template used during synthesis; as a result, the treatment primarily affected the pore openings on the external surface of the crystals, rather than the internal channels. The hierarchical catalysts obtained through chemical etching were used in the catalytic testing (labelled as ETC_25 and ETC_50, according to the Si/Al ratio of the parent material).

A hierarchical MFI zeolite with a nominal silicon-to-aluminum atomic ratio of 25, labelled as HZ_25, was synthesized via a bottom-up

approach. The synthesis began with the preparation of a clear solution by mixing 29.2 g of tetraethyl orthosilicate (TEOS) as the silica source, 1.20 g of aluminum isopropoxide (AIP) as the aluminum source, 13 g of tetrapropylammonium hydroxide (TPAOH, 40 wt% in water) as the structure-directing agent (SDA), and 68 mL of deionized water. This mixture was stirred at ambient temperature for 30 min to ensure complete hydrolysis of the precursors. Following this step, the mixture was heated and maintained under reflux with continuous stirring at 90 °C for 20 h to initiate the formation of the zeolite precursor gel. Afterward, 1.20 g of 3-aminopropyltrimethoxysilane (3-APTMS, 97 %) was added to induce mesoporosity. The mixture was then stirred at 90 °C for an additional 6 h to allow the interaction between the organosilane and the silicate framework. The resulting gel was transferred into a Teflon-lined stainless-steel autoclave and subjected to static hydrothermal crystallization at 170 °C for 5 days. Upon completion, the solid product was recovered by centrifugation, thoroughly washed with deionized water to remove residual organics and ions, and then dried overnight at 60 °C. The dried sample was finally calcined in air at 550 °C for 5 h to remove the organic templates and obtain the final hierarchical zeolite structure. A second hierarchical zeolite with a higher Si/Al ratio (sample HZ_50) was synthesized using the same procedure, with the only modification being the amount of AIP, which was reduced to 0.75 g to achieve the desired aluminum content composition [59,60].

2.2. Characterization of the catalysts

X-ray diffraction (XRD) analysis was carried out using a Miniflex600 diffractometer (Rigaku, Japan) within the 2θ range of 5 ° to 50 °, to assess the crystalline structure of the materials and to evaluate the effect of the post-synthesis treatment on the zeolite crystallinity.

The morphology of the calcined samples was investigated through a field emission scanning electron microscope (FE-SEM) Zeiss Merlin equipped with a Gemini-II column. The samples were covered with a thin layer of Pt (about 5 nm) to enhance their electron conductivity. Besides morphology, the elemental composition was determined via energy-dispersive X-ray spectroscopy (EDS, 15 kV), in selected zones of the catalysts.

Nitrogen adsorption–desorption measurements were conducted at 77 K using a Micromeritics ASAP 2020 porosimeter to evaluate the textural properties of the samples. The surface area was calculated using the BET model within the Rouquerol p/p^0 range. Micropore area was determined via the t-plot method applying the Harkins–Jura thickness equation and considering a thickness range of 3.5–5.0 Å. The pore size distribution was evaluated by applying the DFT method, using the N_2 adsorption kernel at 77 K (oxide cylindrical pores, Tarazona model). Before analysis, the samples were degassed at 350 °C under vacuum (50 μmHg) for 6 h.

Catalyst acidity was assessed via Fourier-transform infrared (FT-IR) spectroscopy, using a Nicolet iS 10 spectrometer (Thermo Scientific, USA) equipped with a DTGS detector. Approximately 25 mg of each zeolite sample was pressed into a 13 mm self-supporting pellet (pressure of 2.7 ton•cm^{-2}) and thermally treated under vacuum at 400 °C for 2 h. Spectra were then recorded at ambient temperature and under high vacuum conditions ($P \approx 10^{-5}$ torr) to analyze the distribution of silanol groups. For a more detailed assessment of surface acidity, the interaction of deuterated acetonitrile (d_3-acetonitrile) with acid sites was studied. The probe molecule was introduced at its vapor pressure and allowed to adsorb at room temperature. After the adsorption, the excess physisorbed d_3-acetonitrile was evacuated until vacuum conditions were re-established ($P \approx 10^{-5}$ torr). The band at 2297 cm^{-1} was attributed to Brønsted acid sites interacting with d_3-acetonitrile, while bands between 2310–2323 cm^{-1} were assigned to Lewis acid sites. The quantity of each type of acid site was estimated by integrating the corresponding IR bands and applying the Lambert-Beer law, using extinction coefficients of $\varepsilon = 2.05$ cm mmol^{-1} (Brønsted sites) and of $\varepsilon = 3.6$ cm mmol^{-1} (Lewis sites) [64]. In order to evaluate the ratio between strong and weak acid sites, the catalysts were characterized by ammonia temperature-programmed desorption (NH_3-TPD) analysis carried out using a TPDRO1100 instrument (Thermo Scientific, USA) equipped with a TCD detector. Approximately 100 mg of dried sample was loaded into a linear quartz microreactor (4 mm internal diameter, 200 mm length) and pretreated in a helium stream (20 mL/min) at 300 °C. After cooling the system to 150 °C, the sample was exposed to an NH_3/He gas mixture (10 % v/v) at the same flow rate for 2 h to ensure full saturation. Subsequently, the physically adsorbed ammonia was removed by flushing with helium at 150 °C until the TCD signal stabilized. Finally, desorption of chemisorbed ammonia was monitored by heating the sample from 100 to 700 °C at a rate of 10 °C/min under a continuous helium flow of 20 mL/min.

The amount of coke deposited over the spent catalysts after catalytic tests was calculated via thermogravimetric analysis (SDT 650, TA Instruments). The produced coke was associated with the weight loss in the temperature range 150–850 °C [65]. A mass of 10 mg of spent zeolite was dissolved using HF, and then soluble coke was extracted using dichloromethane, and the mass spectrometry (GC-MS) analysis provided qualitative information about soluble coke species generated during experimental tests.

2.3. Experimental tests

Dimethyl-ether dehydration tests were carried out in a test bench equipped with a temperature-controlled fixed-bed reactor (see figure S1 for apparatus layout). For each experiment, a mass of 50 mg of fresh calcined zeolite was placed in a quartz tube reactor (inner diameter: 4 mm) and then inserted into a pressure-resistant stainless-steel jacket. The operating temperature was controlled through an electric oven, and a sealed thermocouple was properly placed to measure the temperature of the catalytic bed. Before reaction, the catalyst was pre-treated under an inert flow (5 NTP L·h^{-1} of N_2) at 2 bar and 380 °C (+ 10 °C·min^{-1}) for 2 h. After that, a 14-h endurance test was performed at the selected temperature (namely 300 °C, 325 °C, 350 °C, or 375 °C) and 2 bar by feeding **3 %**vol. DME/N_2 gas mixture from a certified gas cylinder, keeping the condition of 1 g_{cat}·h·mol$_C^{-1}$. The products of the reaction were analyzed by employing a gas chromatograph (7890B GC System, Agilent Technologies) equipped with two columns (HP-5 and HP-PLOT/Q) and two detectors (FID and TCD). Other than the DME conversion, this GC configuration allowed the quantification of methanol, C_2, C_3, C_4, and C_5 hydrocarbon species (both paraffin and olefins). C_{6+} will refer to lumped hydrocarbons with chains longer than 6.

The DME conversion (ζ_{DME}), the product yield (η_i), and the product selectivity (σ_i) were respectively evaluated according to equations (1), (2), and (3).

$$\zeta_{DME} = \frac{\dot{n}_{DME,in} - \dot{n}_{DME,out}}{\dot{n}_{DME,in}} \tag{1}$$

$$\eta_i = \frac{\dot{n}_{C,i,out}}{\dot{n}_{C,DME,in}} = \frac{N_{C,i} \cdot \dot{n}_{i,out}}{N_{C,DME} \cdot \dot{n}_{DME,in}} \tag{2}$$

$$\sigma_i = \frac{\dot{n}_{C,i,out}}{\dot{n}_{C,DME,in} - \dot{n}_{C,DME,out}} = \frac{N_{C,i} \cdot \dot{n}_{i,out}}{N_{C,DME} \cdot (\dot{n}_{DME,in} - \dot{n}_{DME,out})} \tag{3}$$

$\dot{n}$ is the molar flow rate, while $N_{C,i}$ is the number of carbon atoms in the considered species. DTO endurance tests performed at different temperatures allow, at least, apparent kinetic parameters to be estimated. A generic n-th order kinetic reaction rate and a *d*-th order kinetic deactivation rate could be considered, as reported in equations (4) and (5), respectively [66–68].

$$r'_{DME} = -k'_{DME} \cdot C^n_{DME} \cdot a \tag{4}$$

$$\frac{da}{dt} = -k_d \cdot C^m_{DME} \cdot a^d \tag{5}$$

The experimental reactor could be modelled as a plug-flow fixed-bed reactor with a constant flow rate. Under these hypotheses and considering a 1st order kinetic reaction rate ($n = 1$), if a 1st order deactivation rate ($d = 1$) independent of the gas concentration ($m = 0$) is assumed, the DME conversion can be described by equation (6) [66–68]. In addition, the kinetic and deactivation constants can be described through an Arrhenius expression as reported in equations (7).

$$\zeta_{DME} = 1 - \exp\left[-k'_{DME}\cdot\tau'\cdot\exp(-k_d\cdot t)\right] \quad (6)$$

$$\ln\left(k'_{DME}\right) = \ln\left(k'_{DME,T_0}\right) - \frac{E_A}{R}\cdot\left(\frac{1}{T} - \frac{1}{T_0}\right) \quad (7)$$

The kinetic parameters were estimated by minimizing the quadratic residuals between the experimental DME conversion and the modelled DME conversion calculated with equation (6). The objective function (*OF*) of the minimization was described according to equation (8):

$$OF = \min\left[\left(\zeta_{DME,\exp} - \zeta_{DME,\,\mathrm{mod}}\right)^2\right] \quad (8)$$

3. Results and discussion

3.1. Catalyst characterization

Fig. 1 shows the XRD patterns of the catalysts in their acid form. The patterns show that the post-synthetic chemical etching treatment did not compromise the crystallinity of the parent zeolites, which maintained sharp and well-defined diffraction peaks. In contrast, although still crystalline, the hierarchical materials (HZ_25 and HZ_50) synthesized via the bottom-up approach exhibited noticeably lower peak intensities compared to the post-treated samples.

Textural properties of the fresh catalysts are summarized in Table 1, while adsorption/desorption isotherms are reported in Figure S2. All samples exhibited a high specific surface area consistent with an MFI-type zeolite structure. On the one hand, in ETC samples, an increase in the Si/Al ratio led to a decrease in the B.E.T. specific surface area, micropore area, and micropore volume, accompanied by a rise in the external surface area. This trend suggests that higher Si content and the etching treatment promoted the formation of additional mesoporosity, which is consistent with the formation of a mesoporous or sponge-like structure observed in SEM images, as described in the next paragraph. On the other hand, HZ samples showed more similar textural characteristics at the variation of the Si/Al ratio. This indicates that synthesis conditions, particularly the use of the templating agent, better preserved the microporous structure, even at higher Si contents. Figure S3 shows the cumulative pore volume versus the pore size for each sample, suggesting a higher mesoporosity for the zeolites prepared via one-pot synthesis (HZ_25 and HZ_50).

Table 1
Results of the N2 physisorption measurements on the fresh catalysts.

Sample	$S_{B.E.T.}$[a] ($m^2 \cdot g_{cat}^{-1}$)	S_{micro}[b] ($m^2 \cdot g_{cat}^{-1}$)	S_{ext}[b] ($m^2 \cdot g_{cat}^{-1}$)	V_{micro}[c] ($cm^3 \cdot g_{cat}^{-1}$)	V_{tot}[c] ($cm^3 \cdot g_{cat}^{-1}$)
ETC_25	423	263	160	0.202	0.292
ETC_50	374	159	214	0.169	0.271
HZ_25	493	270	223	0.215	0.378
HZ_50	437	302	136	0.202	0.331

[a] Calculated by the multipoint B.E.T. method in the Rouquerol p/p^0 range
[b] Calculated by the t-plot method
[c] Calculated by the DFT method

Fig. 2 presents the SEM images of the fresh ETC and HZ catalysts, highlighting significant morphological differences between the two synthesis routes. ETC samples exhibited two different regions: the first is more irregular (see Fig. 2-a and Fig. 2-c), while the second has well-defined, coffin-shaped crystals (see Fig. 2-b and Fig. 2-d). This dual morphology is likely a result of the etching treatment, which modified surface areas differently for different Si/Al ratios, creating a porous texture alongside the original crystalline domains. It is worth stressing that ETC_25 crystals have sharper edges and more regular facets compared to the smoother and more rounded edges observed in the ETC_50 sample. This difference could be ascribed to the higher Si/Al ratio in ETC_50, which may affect the degree of crystallinity. In contrast, HZ samples are composed of spherical particles with a relatively narrow size distribution, centered around 300 nm, formed by the aggregation of small, coalesced grains (see Fig. 2-e and Fig. 2-f). The different morphology of HZ samples compared to ETC samples was ascribed to the use of a different structure-directing agent for the synthesis. The elemental distribution in all calcined samples was analyzed through SEM-EDS maps of different areas of the samples. The distribution of Si,

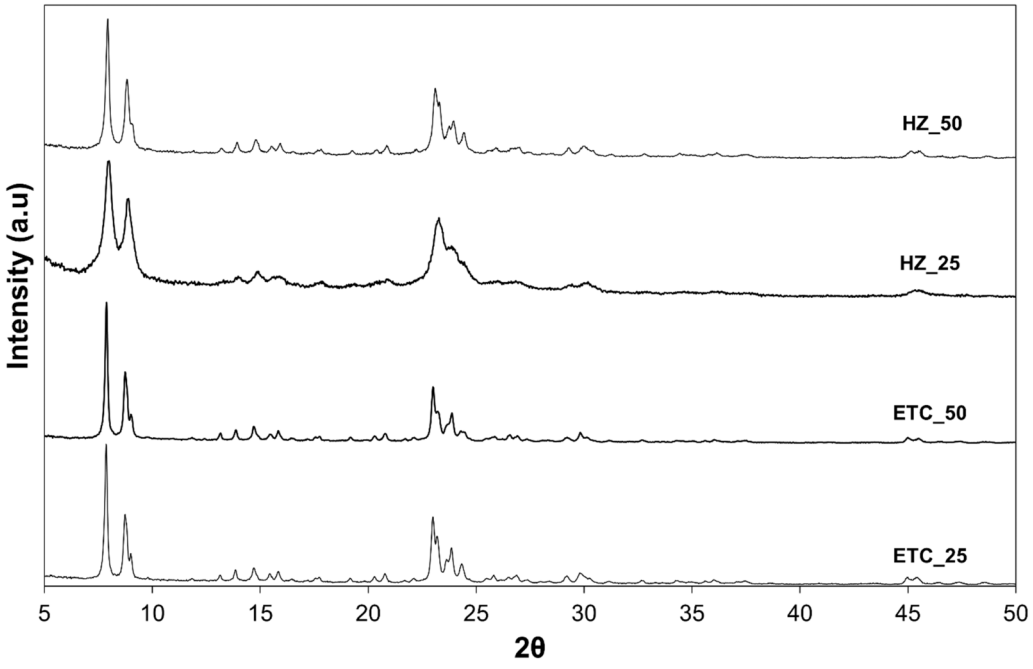

Fig. 1. XRD patterns of the investigated samples. For the sake of clarity, diffractograms are stacked to avoid overlapping.

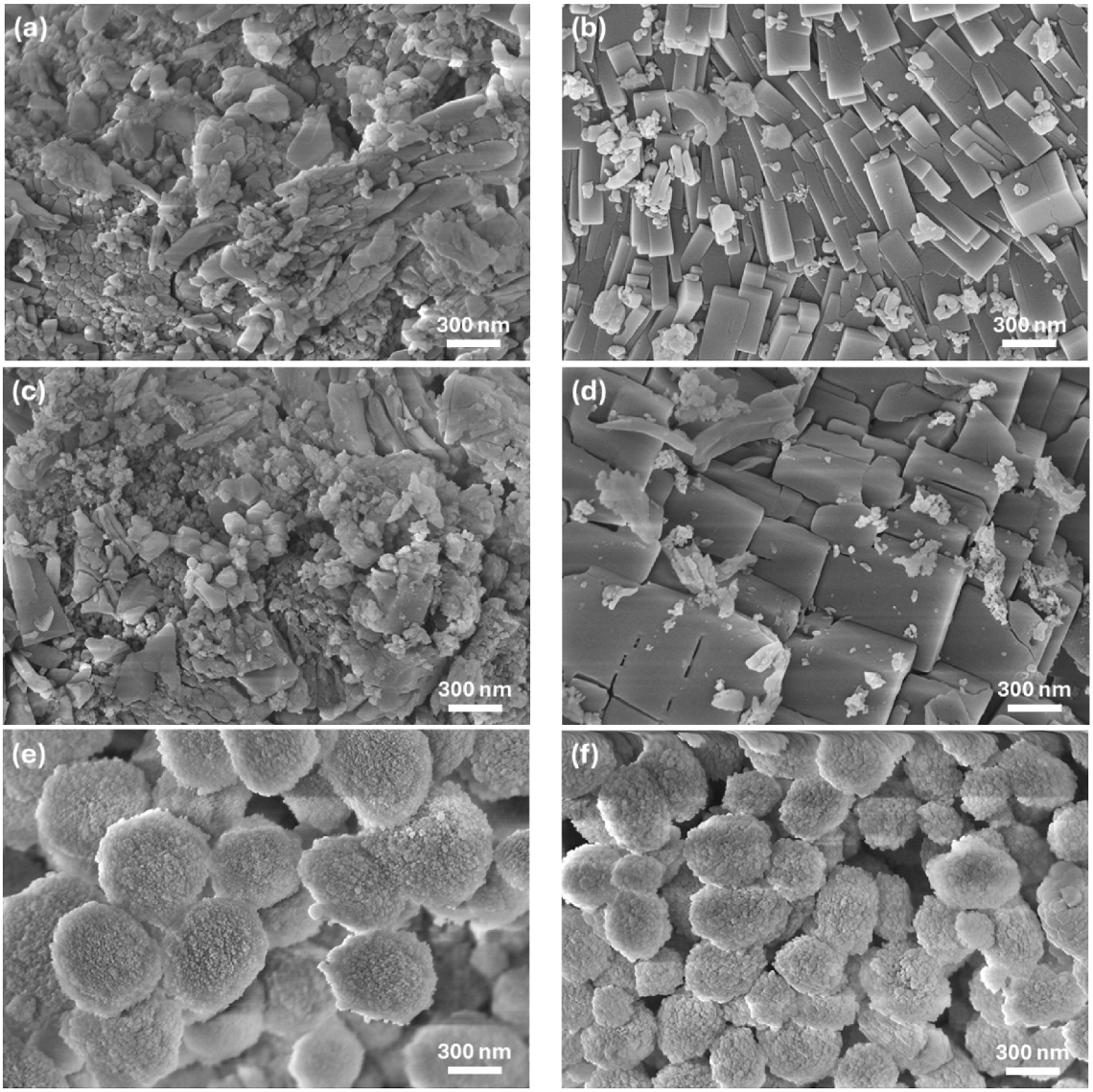

Fig. 2. FE-SEM images of fresh (a, b) ETC_25, (c, d) ETC_50 catalysts, (e) HZ_25, and (f) HZ_50 (magnification: 100 kX).

O, and Al was uniform and homogeneous in all samples for all areas (Figure S4-S7).

Figure S8 shows the FT-IR spectra in the OH stretching region (3800–3000 cm^{-1}), recorded at room temperature following a 2-hour pre-treatment at 400 °C under vacuum. All FT-IR spectra shown have been normalized with respect to the pellet density calculated as the mass of the pellet divided by the area of the disk (with a radius of 13 mm). In all samples, a band at approximately 3745 cm^{-1} was observed, attributed to silanol groups on the external surface of the catalysts [69]. HZ_25 and HZ_50 samples seem to be the catalysts with the highest concentration of silanols. Additionally, a broader band around 3610 cm^{-1}, associated with acidic bridging Si-(OH)-Al groups, was detected in each sample and exhibited higher intensity in ETC_25 and ETC_50 catalysts. A further band at 3660 cm^{-1} was particularly observed in the ETC_25 sample. This band is attributed to the presence of extra-framework Al–OH species [70]. Finally, a small band at around 3780 cm^{-1} was detected for the ETC_25 sample, with this band attributed to weak OH groups on extra-framework debris [70]. Figure S9 shows FT-IR spectra in the OH-region recorded after d_3-acetonitrile adsorption and 1 h outgassing at 150 °C. The figure highlights acid sites interactions with the probe molecule. The bands at 3610 and 3660 cm^{-1} disappeared, indicating that both Si–OH–Al bridges and extra-framework aluminum species interact with deuterated acetonitrile. Meanwhile, the 3735 cm^{-1} band, corresponding to silanol groups on the external surface, remained largely unchanged, indicating that these weaker groups do not participate in the interaction.

Figure S10 shows the spectra obtained after the interaction of the analyzed samples with d_3-acetonitrile in the wavenumber range 2400–2200 cm^{-1}. Two main bands were observed: the first at 2320 cm^{-1}, assigned to d_3-acetonitrile coordinated to Lewis acid sites; the second at 2290 cm^{-1}, corresponding to Brønsted acid sites.

The acid properties of the fresh samples are summarized in Table 2. In both series (i.e., ETC and HZ), increasing the nominal Si/Al ratio led

Table 2
Acid sites distribution of the fresh catalysts.

Sample	Si/Al[a]	BAS[b] ($\mu mol \cdot g_{cat}^{-1}$)	LAS[b] ($\mu mol \cdot g_{cat}^{-1}$)	BAS+LAS ($\mu mol \cdot g_{cat}^{-1}$)	BAS/LAS
ETC_25	15.3	259	116	375	2.2
ETC_50	24.8	203	85	288	2.4
HZ_25	19.9	159	147	306	1.1
HZ_50	34.4	178	108	286	1.6

[a] evaluated using SEM-EDS elemental maps.
[b] evaluated using FT-IR spectroscopy with D_3-acetonitrile as a probe molecule.

to an increase in the actual one, consistent with a successful modulation of the framework composition. In addition, a decrease in total and Lewis acid sites (LAS) was observed, confirming that higher SiO_2 content leads to a lower acidity of the samples, particularly affecting the concentration of LAS. The Brønsted-to-Lewis acid site (BAS/LAS) ratio increased with the Si/Al ratio in both series, indicating a relative enrichment of Brønsted acidity, which did not have a consistent trend with a rising Si/Al ratio, suggesting that it may be less sensitive to framework composition or influenced by other structural factors. Overall, while the Si/Al ratio approximately doubled, the total acidity decreased only slightly. This behavior may be ascribed to the higher framework stability at lower aluminum content, where the amount of framework Al, and thus Brønsted sites, remains nearly constant, whereas extra-framework Al, responsible for Lewis sites, decreases significantly.

The profiles from NH3-TPD analysis are reported for each sample in Figure S11. All the analyzed samples exhibited the characteristic desorption profile of MFI-type zeolites, featuring a low-temperature peak (100–350 °C) associated with ammonia desorption from weak acid sites and a high-temperature peak (300–550 °C) related to strong acid sites [71]. The peak temperatures are indicated in the figures. By comparing samples prepared using the same procedure, it is evident that, regardless of the specific synthesis method, those with a higher Si/Al ratio in the gel exhibited a lower total acidity. To gain insights into the ratio between strong and weak acid sites, peak deconvolution was performed using Peakfit software, and the corresponding area ratios were calculated. The results, expressed as μmol of ammonia per gram of catalyst, are summarized in Table S1 in the Supporting Information. These data have then been used to determine the ratio between strong and weak acid sites. Results revealed that, unlike the other samples, whose ratios consistently remained around 2.5, the HZ_25 sample exhibited a higher value (≈4.2), indicating a greater proportion of strong acid sites per gram of catalyst.

3.2. DTO catalytic tests

The catalytic behavior of the hierarchical zeolites was evaluated by performing stability tests at different temperatures. As can be seen by comparing data from 300 °C to 350 °C (Figures S12-S15) and data at 375 °C (Fig. 3), all catalysts exhibited an increase in DME conversion as the temperature rose, reaching values of approximately 90 % at 375 °C. In more detail, ETC_25 showed a DME conversion increase from 15 % at 300 °C to nearly 90 % at 375 °C, while the HZ_25 was slightly less active under the same reaction conditions. During the tests, ETC_50 and HZ_50 exhibited similar DME conversion trends. Despite a similar total

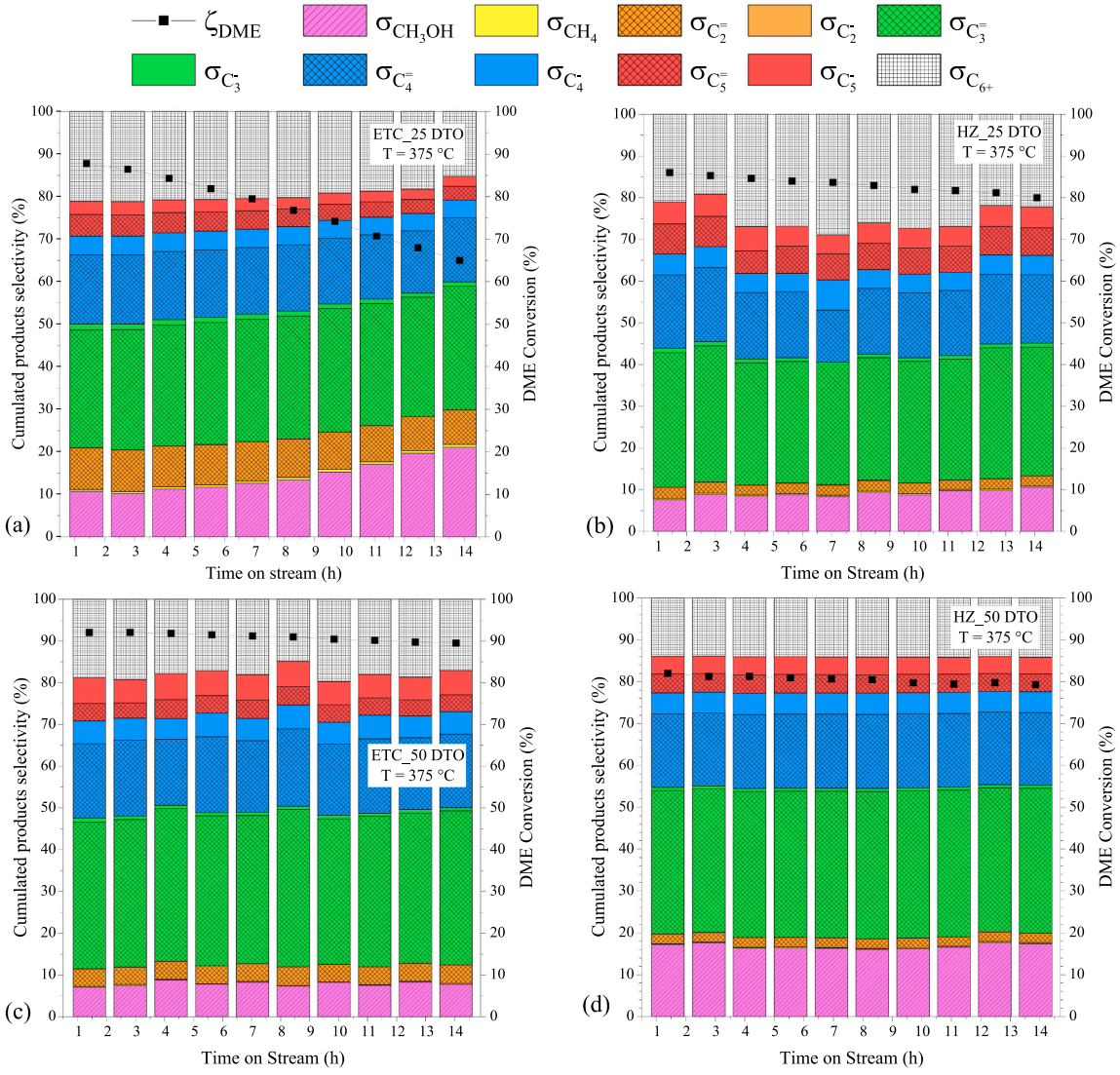

Fig. 3. Time-on-stream DTO tests at 375 °C with different zeolites: (a) ETC_25, (b) HZ_25, (c) ETC_50 and (d) HZ_50. Reaction conditions: 2 bar and 1 $g_{cat} \cdot h \cdot mol_C^{-1}$ using **3 %**vol. DME/N_2.

concentration of acid sites, ETC_50 presented higher DME conversion than HZ_50, suggesting that the global conversion may be affected not only by the acidity (and the nature of acid sites) but also by textural and structural properties. Furthermore, ETC_50 presents a higher concentration of BAS than HZ_50. The arene cycle of the dual cycle hydrocarbon pool mechanism is favored by Brønsted acid sites. If alkene and arene cycles occur in parallel, a different distribution between Brønsted and Lewis acid centers may also affect the reactant conversion besides the product selectivity.

According to NH_3-TPD characterization, ETC_50 shows a slightly greater amount of strong acid sites than HZ_50 (ratio S/W of 2.8 vs. 2.4), which may be partly responsible for the higher reactant conversion. As shown in Fig. 3, stability tests revealed significant differences at 375 °C: HZ_25 exhibited a more stable performance compared to ETC_25, with a lower decrease in activity. In addition, the high Si/Al ratio enhanced the stability of both samples, mitigating the deactivation.

Hydrocarbon selectivity was strongly influenced by both reaction temperature and catalyst morphology. ETC materials, characterized by a more compact and microporous structure, favored the formation of light olefins (C_2-C_4) at lower temperatures, while at higher temperatures, heavier hydrocarbons (mainly C_{5+}) were produced. In contrast, HZ catalysts exhibited lower olefin formation and revealed a lower ethylene selectivity and higher C_3-C_5 selectivity in all reaction conditions compared to ETC samples. The lower amount of C_2H_4 produced by HZ_25/HZ_50 samples may be related to a shape selectivity effect, as the pore size distribution is more oriented towards mesopores. Another aspect to take into account is related to the different distribution of acid sites between Brønsted and Lewis types. Zeolites prepared via the one-pot synthesis (HZ_25 and HZ_50) present a greater share of LAS (see Table 2), which could affect the ethylene production occurring via the aromatic cycle of the hydrocarbon pool mechanism, while the heavier olefins are generated through the alkene cycle via methylation and cracking steps. According to the open literature, aromatic species formation and reaction are favored by the presence of Brønsted acid sites, whilst a greater amount of Lewis acid sites would enhance the production of olefins like propene and heavier, generated through the olefin cycle [72]. Aromatics already produced via the arene cycle may thus undergo dealkylation preferentially over Brønsted acid sites. Therefore, the lower ethylene selectivity for HZ_25 and HZ_50 can be partly explained by their lower BAS/LAS ratio.

Methanol selectivity increased as the DME conversion decreased, consistent with the fast kinetics of the rehydration step. HZ catalysts consistently exhibited a greater P/E ratio compared to their ETC counterparts. Moreover, catalysts with a lower Si/Al ratio showed faster deactivation, highlighting the role of the acid site density in stability. Lastly, the hierarchization method significantly affected the hydrocarbon product distribution, particularly in terms of ethylene and propylene yields.

The enhanced catalytic performance of hierarchical zeolites is evident when compared with that of their parent zeolites, as reported in our previous work. Although parent zeolites showed higher initial activity and reached nearly complete DME conversion at high temperature (i.e., 375 °C), they underwent rapid deactivation, in some cases halving their activity within the same time on stream period [58]. In contrast, hierarchical zeolites exhibit evidently improved stability under analogous reaction conditions.

More in detail, the initial light olefins ($C_{2=}$-$C_{4=}$) selectivity, evaluated at the first sampling of the reacted gas mixture and reported in Table 3, increases as the reaction temperature rises, reflecting the favored dehydration process at higher temperatures. As far as ETC samples are concerned, ETC_50 consistently outperformed ETC_25, indicating that the higher Si/Al ratio and modifications induced by the etching treatment (i.e., higher BAS/LAS ratio, lower overall acidity, and increased mesoporosity) favor the selective formation of light olefins. In addition, the maximum value of olefins selectivity was identified at 350 °C for both ETC samples. On the contrary, HZ samples exhibited a less evident difference between the two samples, suggesting that the more uniform morphology and microporosity mitigate the impact on the olefin selectivity. Hence, the synthesis technique affects the light olefins distribution.

As the main olefin product of DME dehydration is propylene, a focus on C_3H_6 is thus crucial. The performance of all catalysts in terms of propylene production at 375 °C is summarized in Table 4. ETC_50 stands out with the highest propylene yield and production, outperforming even the parent zeolite (i.e., ZSM5_50), as reported in the literature [58]. These results confirm the beneficial effects of etching treatment and increased Si/Al ratio, which led to enhanced external surface area and a higher BAS/LAS ratio, both of which promoted propylene formation. In particular, the higher propylene yield of ETC_50 compared to ETC_25 can be partly linked to its higher BAS/LAS and the abundance of BAS in the more diffusion-limited ETC structure. On the contrary, HZ catalysts did not reach that level of performance, due to different acid site distribution and morphology. HZ samples indeed have a more open and interconnected porosity that reduces the diffusional limitation, mitigating the effect of the relative abundance of acid sites. Accordingly, the higher BAS/LAS ratio did not lead to enhanced propylene production. This indicates that the effect of BAS/LAS on catalytic performance also depends on the specific textural properties of the catalyst. The effect of

Table 3
Initial light olefins (C2 $_=$ - C4 $_=$) selectivity evaluated at the 1 st gas sampling during each TOS (averaged values are reported between brackets). Selectivity is evaluated in terms of converted C atoms.

Sample	300 °C	325 °C	350 °C	375 °C
ETC_25	37.5 % (36.6 %)	44.6 % (43.6 %)	56.6 % (53.0 %)	53.8 % (53.2 %)
ETC_50	**47.0 %** (41.9 %)	**58.3 %** (49.9 %)	60.0 % (58.5 %)	57.2 % (57.9 %)
HZ_25	39.0 % (39.3 %)	47.5 % (44.5 %)	52.4 % (49.4 %)	53.5 % (49.7 %)
HZ_50	35.2 % (34.4 %)	40.2 % (39.8 %)	49.4 % (49.2 %)	54.2 % (54.7 %)

Table 4
Propylene yield and productivity during TOS at 375 °C. For the sake of clarity, C3H6 yield and C3H6 specific productivity were evaluated at the first gas sampling during TOS (the averaged values are reported between brackets).

Sample	C_3H_6 yield (%)	C_3H_6 specific productivity ($mol_{C3H6} \cdot kg_{cat}^{-1} \cdot h^{-1}$)	Total C_3H_6 productivity ($g_{C3H6} \cdot g_{cat}^{-1}$)
ETC_25	24.3 (22.1)	82.7 (75.1)	43.5
ETC_50	32.4 (32.8)	107.9 (109.1)	75.1
HZ_25	28.3 (25.7)	95.3 (86.4)	51.4
HZ_50	28.1 (28.0)	95.1 (94.7)	55.3

Table 5
Kinetic parameters for DTO process assuming n = 1, m = 0, d = 1 and T0 = 300 °C.

Sample	k'_{DME,T_0} (mol · kg^{-1} · h^{-1})	E_A (kJ · mol^{-1})	k_{d,T_0} (h^{-1})	E_d (kJ · mol^{-1})	*OF*
ETC_25	$8.33 \cdot 10^{1}$	108.6	$8.89 \cdot 10^{-4}$	186.8	$4.77 \cdot 10^{-2}$
ETC_50	$8.55 \cdot 10^{1}$	114.5	$5.64 \cdot 10^{-8}$	550.5	$1.24 \cdot 10^{-2}$
HZ_25	$5.07 \cdot 10^{1}$	113.7	$2.47 \cdot 10^{-4}$	179.2	$1.26 \cdot 10^{-3}$
HZ_50	$7.45 \cdot 10^{1}$	96.2	$5.03 \cdot 10^{-8}$	534.6	$9.24 \cdot 10^{-3}$

the Si/Al ratio on stability is also evident: the main difference between the first and the average value during TOS occurs for samples with a lower Si/Al ratio, as they are more affected by deactivation.

Tables S2-S4 in the Supporting Material provide insights into catalyst performance and propylene production during TOS. Those data also confirm a clear temperature-dependent increase in propylene production, particularly for the ETC samples. This behavior highlights the effectiveness of tuning both acidity and porosity to optimize light olefins production from DME.

Table S5 reports the propylene-to-ethylene (P/E) ratio for all the tests, calculated as the ratio between the molar flow rate of C_3H_6 and C_2H_4. As already pointed out before, the two hierarchical samples synthesized through a bottom-up approach (HZ_25 and HZ_50) show a considerably higher value of P/E at each temperature; the alkene cycle of the hydrocarbon pool mechanism seems to be thus favored for these samples.

The results of simplified kinetic modelling (summarized in Table 5) further support the discussed experimental findings, thus highlighting the influence of both catalyst composition and structure on activity and stability. The apparent pre-exponential factor of the DME reaction rates suggests that ETC samples have more active sites than HZ samples; this is consistent with the measurements of both the Si/Al ratios and the Brønsted acidity of the samples. Figure S16 presents

the calculated k'_{DME,T_0} as a function of the acid properties of the samples. In more detail, the pre-exponential factor increases at greater BAS/LAS, while it decreases as the LAS rises. As the amount of total acid sites (BAS+LAS) is comparable for all samples, it may be inferred that the conversion of dimethyl ether may occur (at least preferentially) on Brønsted acid sites. Furthermore, ETC samples exhibited an apparent activation energy (E_A) slightly higher than HZ samples, suggesting that mass transport is facilitated in HZ samples. This fact was ascribed to the different hierarchization techniques, but the acidity concentration seems to prevail over the mass transport limitations. Concerning the stability of the hierarchical samples, those with a higher Si/Al ratio (i.e., ETC_50 and HZ_50) showed significantly lower deactivation rates and higher energies of deactivation, confirming an improved long-term stability. It is worth noting that the pre-exponential factor for DME dehydration (k'_{DME,T_0}) increased with the BAS/LAS ratio, suggesting that a higher relative abundance of BAS favors the dehydration process. In contrast, it also decreased as the concentration of LAS increased, implying a possible inhibition effect of LAS due to the stabilization of intermediates (e.g., heavy aromatics in the hydrocarbon pool). No evident trends were observed between acidity and other kinetic parameters, indicating that they may be governed by other factors rather than solely by acid site characteristics.

3.3. Spent catalysts characterization

Table 6 summarizes the specific coke production per unit of converted DME during TOS at different reaction temperatures. It is worth noting that it decreases by reducing the acidity of the samples, and it is also lower than the specific coke production on the MFI-type parent zeolites [58]. The samples exhibited a minimum specific coke production at intermediate temperatures (325–350 °C), which may be related to a temperature-dependent balance between DME conversion rate and product distribution. The selectivity toward light olefins is rising, and aromatization, which is responsible for the formation of coke precursors, is not yet favored. At higher temperatures (i.e., T > 350 °C), the formation of heavy hydrocarbons becomes more important, increasing the amount of deposited coke, especially on strong acid sites. On the contrary, lower temperatures (T < 325 °C) may lead to longer residence times of intermediates, favoring condensation pathways and slowing down their desorption from the surface of the catalyst.

Those results could be rationalized by considering the acidity and the morphology of the samples. ETC samples produced less coke than HZ samples. More in detail, ETC_50 showed the lowest specific coke production that could be ascribed to the low density of acid sites, high BAS/LAS ratio, and a more open mesoporous structure. On the contrary, ETC_25 and HZ samples exhibited highly specific coke productions that were attributed to a more microporous structure of the samples, as can be seen in Table 1. In addition, a higher acidity of the samples favors catalytic activity and the formation of heavy hydrocarbons that occlude the pores and quickly deactivate the catalyst. In conclusion, the mesoporous structure obtained through the etching treatment seems to be more efficient for mitigating coke formation and improving propylene productivity, but micropores are still progressively clogged by heavy species that reduce DME conversion during TOS. On the contrary, the hierarchization technique did not avoid coking, but the wider and more homogeneous porosities keep the DME conversion high under all reaction conditions, exhibiting slow deactivation rates.

Figure S17 shows the chromatograms referring to the spent ETC_25 and HZ_50 samples (both tested at 350 °C). The two most abundant soluble coke species that were detected are pentamethylbenzene and hexamethylbenzene. Similar results were obtained for all the spent samples.

4. Conclusion

Two different synthesis techniques were used to obtain hierarchical zeolites with MFI structure, and samples were tested in the conversion of dimethyl ether (DME) into olefins (DTO). The first one was a post-treatment of the HZM-5 sample with NH_4F and HF with the scope to etch the zeolite surface (ETC), whilst the second one involved the use of an additional organic structure directing agent (3-APTMS) during the synthesis (HZ). Both procedures were used to synthesize samples with different silicon-to-aluminum ratios, leading to the production of samples labelled as ETC_25, ETC_50, HZ_25, and HZ_50.

Pore size distribution revealed that both the synthesis techniques were effective in inducing hierarchization. Moreover, HZ_25 and HZ_50 catalysts resulted in a lower ratio (1.1 and 1.6, respectively) between Brønsted and Lewis acid sites concentration (BAS/LAS).

Table 6
Specific coke production referred to the overall converted DME during TOS (expressed in $\boldsymbol{mg_{coke} \cdot g^{-1}_{DME,conv}}$).

Sample	300 °C	325 °C	350 °C	375 °C
ETC_25	0.612	0.197	0.153	0.205
ETC_50	0.257	0.093	0.072	0.143
HZ_25	0.826	0.345	0.194	0.180
HZ_50	0.672	0.297	0.184	0.191

At increasing temperature, the zeolites showed a slightly reduced stability, especially the ones characterized by greater acidity. For instance, DME conversion at 375 °C with ETC_25 changed from 87.8 % to 65.0 % over 14 h of time-on-stream, whilst the other samples presented superior stability. At low temperature, methanol selectivity is higher, due to faster kinetics for the methanol/DME reaction. Samples prepared via etching (ETC_25 and ETC_50) resulted in a higher light olefin ($C_{2=}$ - $C_{4=}$) selectivity (up to about 58 %). On the other hand, hierarchical zeolites prepared through the bottom-up approach (HZ_25 and HZ_50) showed improved stability. Furthermore, these latter samples produced a hydrocarbon mixture with a very low amount of ethylene and a larger C_3H_6/C_2H_4 ratio (P/E), due to a different shape selectivity and a different extent of the two cycles that constitute the hydrocarbon pool mechanism, partly related to a different distribution among Brønsted and Lewis acidity.

The investigation revealed that tuning the MFI zeolites via hierarchization is an effective strategy to generate more stable catalysts in the DTO process. Future studies should be focused on providing more insights into the relationship between structure/acidity and stability/product distribution, and potentially in the conversion of methanol into olefins (MTO).

CRediT authorship contribution statement

Fabio Salomone: Writing – original draft, Visualization, Software, Investigation, Formal analysis, Data curation. **Giorgia Ferrarelli:** Writing – original draft, Methodology, Investigation, Data curation. **Emanuele Giglio:** Writing – original draft, Methodology, Investigation, Formal analysis, Data curation. **Elena Corrao:** Writing – original draft, Methodology, Investigation. **Massimo Migliori:** Writing – review & editing, Resources, Formal analysis, Conceptualization. **Samir Bensaid:** Supervision, Resources, Formal analysis. **Raffaele Pirone:** Validation, Supervision, Funding acquisition. **Girolamo Giordano:** Supervision, Project administration, Funding acquisition.

Declaration of Competing Interest

The authors declare that they have no known competing financial interests or personal relationships that could have appeared to influence the work reported in this paper.

Appendix A. Supporting information

Supplementary data associated with this article can be found in the online version at doi:10.1016/j.cattod.2025.115618.

Data availability

Data will be made available on request.

References

[1] A. Kumler, B. Kravitz, C. Draxl, L. Vimmerstedt, B. Benton, J.K. Lundquist, M. Martin, H.J. Buck, H. Wang, C. Lennard, L. Tao, Potential effects of climate change and solar radiation modification on renewable energy resources, Renew. Sustain. Energy Rev. 207 (2025) 114934, https://doi.org/10.1016/j.rser.2024.114934.

[2] Z. Huang, W. Zhang, D. Han, L. Zhu, H. Lin, B. Guan, Dimethyl ether: a promising fuel for marine engines, Front. Energy 19 (2025) 28–32, https://doi.org/10.1007/s11708-025-0986-4.

[3] P. Tyagi, M. Kapur, V. Kumar, Postcombustion carbon dioxide gas conversion to methanol and dimethyl ether, in: in: Sustainable and Green Catalytic Processes for Renewable Fuel Production with Net-Zero Emissions, Elsevier, 2025, pp. 83–115, https://doi.org/10.1016/B978-0-443-21899-6.00004-5.

[4] K. Faungnawakij, K. Eguchi, Dimethyl Ether—Reforming Catalysts for Hydrogen Production, Catal. Surv. Asia 15 (2011) 12–24, https://doi.org/10.1007/s10563-010-9103-7.

[5] K. Mansouri, F. Bahmanzadegan, A. Ghaemi, Evaluation of hydrogen production via steam reforming and partial oxidation of dimethyl ether using response surface methodology and artificial neural network, Sci. Rep. 14 (2024) 15570, https://doi.org/10.1038/s41598-024-66402-5.

[6] S.S. Tabibian, M. Sharifzadeh, Statistical and analytical investigation of methanol applications, production technologies, value-chain and economy with a special focus on renewable methanol, Renew. Sustain. Energy Rev. 179 (2023) 113281, https://doi.org/10.1016/j.rser.2023.113281.

[7] S.H. Park, C.S. Lee, Applicability of dimethyl ether (DME) in a compression ignition engine as an alternative fuel, Energy Convers. Manag 86 (2014) 848–863, https://doi.org/10.1016/j.enconman.2014.06.051.

[8] C. Arcoumanis, C. Bae, R. Crookes, E. Kinoshita, The potential of di-methyl ether (DME) as an alternative fuel for compression-ignition engines: A review, Fuel 87 (2008) 1014–1030, https://doi.org/10.1016/j.fuel.2007.06.007.

[9] H. Zimmermann, R. Walzl, Ethylene, in: in: Ullmann's Encyclopedia of Industrial Chemistry, Wiley-VCH Verlag GmbH & Co. KGaA, Weinheim, Germany, 2009, https://doi.org/10.1002/14356007.a10_045.pub3.

[10] H. Zimmermann, Propene, in: in: Ullmann's Encyclopedia of Industrial Chemistry, Wiley, 2013, https://doi.org/10.1002/14356007.a22_211.pub3, pp. 00–00.

[11] F.M.A. Geilen, G. Stochniol, S. Peitz, E. Schulte-Koerne, Butenes, in: in: Ullmann's Encyclopedia of Industrial Chemistry, Wiley, 2014, pp. 1–13, https://doi.org/10.1002/14356007.a04_483.pub3.

[12] Statista. Production capacity of ethylene worldwide from 2018 to 2023 , (n.d.). https://www.statista.com/statistics/1067372/global-ethylene-production-capacity/ (accessed June 29, 2025)..

[13] Statista. Production capacity of propylene worldwide from 2018 to 2023, with a forecast to 2030, (n.d.). https://www.statista.com/statistics/1065879/global-propylene-production-capacity/ (accessed June 29, 2025)..

[14] ChemAnalyst. Ethylene Market Analysis. Decode the Future of Ethylene, (n.d.). https://www.chemanalyst.com/industry-report/ethylene-market-638 (accessed June 29, 2025)..

[15] P. Shirzad, I. Kantor, Toward sustainable propylene: A comparison of current and future production pathways, Renew. Sustain. Energy Transit. 7 (2025) 100099, https://doi.org/10.1016/j.rset.2024.100099.

[16] N.S. Almuqati, A.M. Aldawsari, K.N. Alharbi, S. González-Cortés, M.F. Alotibi, F. Alzaidi, J.R. Dilworth, P.P. Edwards, Catalytic production of light Olefins: Perspective and prospective, Fuel 366 (2024) 131270, https://doi.org/10.1016/j.fuel.2024.131270.

[17] S.N. Khadzhiev, M.V. Magomedova, E.G. Peresypkina, Mechanism of olefin synthesis from methanol and dimethyl ether over zeolite catalysts: A review, Pet. Chem. 54 (2014) 245–269, https://doi.org/10.1134/S0965544114040057.

[18] P. Pérez-Uriarte, A. Ateka, M. Gamero, A.T. Aguayo, J. Bilbao, Effect of the Operating Conditions in the Transformation of DME to olefins over a HZSM-5 Zeolite Catalyst, Ind. Eng. Chem. Res 55 (2016) 6569–6578, https://doi.org/10.1021/acs.iecr.6b00627.

[19] T. Cordero-Lanzac, A.G. Gayubo, A.T. Aguayo, J. Bilbao, The MTO and DTO processes as greener alternatives to produce olefins: A review of kinetic models and reactor design, Chem. Eng. J. 494 (2024) 152906, https://doi.org/10.1016/j.cej.2024.152906.

[20] S. Lin, H. Li, P. Tian, Y. Wei, M. Ye, Z. Liu, Methanol to Olefins (MTO): Understanding and Regulating Dynamic Complex Catalysis, J. Am. Chem. Soc. (2025), https://doi.org/10.1021/jacs.4c12145.

[21] D. Parigi, E. Giglio, A. Soto, M. Santarelli, Power-to-fuels through carbon dioxide Re-Utilization and high-temperature electrolysis: A technical and economical comparison between synthetic methanol and methane, J. Clean. Prod. 226 (2019) 679–691, https://doi.org/10.1016/j.jclepro.2019.04.087.

[22] M. Marchese, N. Heikkinen, E. Giglio, A. Lanzini, J. Lehtonen, M. Reinikainen, Kinetic Study Based on the Carbide Mechanism of a Co-Pt/γ-Al_2O_3 Fischer–Tropsch Catalyst Tested in a Laboratory-Scale Tubular Reactor, Catalysts 9 (2019) 717, https://doi.org/10.3390/catal9090717.

[23] A. De Padova, E. Giglio, M. Santarelli, Electrolysis-boosted substitute natural gas from biomass: Kinetic modeling of fluidized bed gasification and system integration, Renew. Energy 223 (2024) 120071, https://doi.org/10.1016/j.renene.2024.120071.

[24] E. Giglio, M. Bianco, G. Zanardi, E. Catizzone, G. Giordano, M. Migliori, Direct biogas methanation via renewable-based Power-to-Gas: Techno-economic assessment based on real industrial data, Energy Convers. Manag 332 (2025) 119775, https://doi.org/10.1016/j.enconman.2025.119775.

[25] C. Cara, F. Secci, S. Lai, V. Mameli, K. Skrodczky, P.A. Russo, F. Ferrara, E. Rombi, N. Pinna, M. Mureddu, C. Cannas, On the design of mesostructured acidic catalysts for the one-pot dimethyl ether production from CO_2, J. CO2 Util. 62 (2022) 102066, https://doi.org/10.1016/j.jcou.2022.102066.

[26] A. Ateka, P. Rodriguez-Vega, J. Ereña, A.T. Aguayo, J. Bilbao, A review on the valorization of CO_2. Focusing on the thermodynamics and catalyst design studies of the direct synthesis of dimethyl ether, Fuel Process. Technol. 233 (2022) 107310, https://doi.org/10.1016/j.fuproc.2022.107310.

[27] E. Catizzone, C. Freda, G. Braccio, F. Frusteri, G. Bonura, Dimethyl ether as circular hydrogen carrier: Catalytic aspects of hydrogenation/dehydrogenation steps, J. Energy Chem. 58 (2021) 55–77, https://doi.org/10.1016/j.jechem.2020.09.040.

[28] E. Catizzone, E. Giglio, M. Migliori, P.C. Cozzucoli, G. Giordano, The Effect of Zeolite Features on the Dehydration Reaction of Methanol to Dimethyl Ether: Catalytic Behaviour and Kinetics, Materials 13 (2020) 5577, https://doi.org/10.3390/ma13235577.

[29] S. Ilias, A. Bhan, Mechanism of the Catalytic Conversion of Methanol to Hydrocarbons, ACS Catal. 3 (2013) 18–31, https://doi.org/10.1021/cs3006583.

[30] S. Ilias, R. Khare, A. Malek, A. Bhan, A descriptor for the relative propagation of the aromatic- and olefin-based cycles in methanol-to-hydrocarbons conversion on H-ZSM-5, J. Catal. 303 (2013) 135–140, https://doi.org/10.1016/j.jcat.2013.03.021.

[31] M. Bjørgen, S. Svelle, F. Joensen, J. Nerlov, S. Kolboe, F. Bonino, L. Palumbo, S. Bordiga, U. Olsbye, Conversion of methanol to hydrocarbons over zeolite H-ZSM-5: On the origin of the olefinic species, J. Catal. 249 (2007) 195–207, https://doi.org/10.1016/j.jcat.2007.04.006.
[32] F.M. Kirchberger, Y. Liu, P.N. Plessow, M. Tonigold, F. Studt, M. Sanchez-Sanchez, J.A. Lercher, Mechanistic differences between methanol and dimethyl ether in zeolite-catalyzed hydrocarbon synthesis, Proc. Natl. Acad. Sci. 119 (2022), https://doi.org/10.1073/pnas.2103840119.
[33] P. Pérez-Uriarte, A. Ateka, A.T. Aguayo, A.G. Gayubo, J. Bilbao, Kinetic model for the reaction of DME to olefins over a HZSM-5 zeolite catalyst, Chem. Eng. J. 302 (2016) 801–810, https://doi.org/10.1016/j.cej.2016.05.096.
[34] S. Wang, Z. Qin, M. Dong, J. Wang, W. Fan, Recent progress on MTO reaction mechanisms and regulation of acid site distribution in the zeolite framework, Chem. Catal. 2 (2022) 1657–1685, https://doi.org/10.1016/j.checat.2022.05.012.
[35] D. Zhao, Y. Zhang, Z. Li, Y. Wang, J. Yu, Synthesis of SAPO-18/34 intergrowth zeolites and their enhanced stability for dimethyl ether to olefins, RSC Adv. 7 (2017) 939–946, https://doi.org/10.1039/c6ra25080g.
[36] Y. Cui, Q. Zhang, J. He, Y. Wang, F. Wei, Pore-structure-mediated hierarchical SAPO-34: Facile synthesis, tunable nanostructure, and catalysis applications for the conversion of dimethyl ether into olefins, Particuology 11 (2013) 468–474, https://doi.org/10.1016/j.partic.2012.12.009.
[37] Y. Hirota, K. Murata, M. Miyamoto, Y. Egashira, N. Nishiyama, Light olefins synthesis from methanol and dimethylether over SAPO-34 nanocrystals, Catal. Lett. 140 (2010) 22–26, https://doi.org/10.1007/s10562-010-0421-1.
[38] M. Ghavipour, R.M. Behbahani, R.B. Rostami, A.S. Lemraski, Methanol/dimethyl ether to light olefins over SAPO-34: Comprehensive comparison of the products distribution and catalyst performance, J. Nat. Gas. Sci. Eng. 21 (2014) 532–539, https://doi.org/10.1016/j.jngse.2014.09.015.
[39] D. Zhao, Y. Zhang, Z. Li, Y. Wang, J. Yu, Synthesis of AEI/CHA intergrowth zeolites by dual templates and their catalytic performance for dimethyl ether to olefins, Chem. Eng. J. 323 (2017) 295–303, https://doi.org/10.1016/j.cej.2017.04.109.
[40] A.S. Al-Dughaither, H. De Lasa, Neat dimethyl ether conversion to olefins (DTO) over HZSM-5: Effect of SiO_2/Al_2O_3 on porosity, surface chemistry, and reactivity, Fuel 138 (2014) 52–64, https://doi.org/10.1016/j.fuel.2014.07.026.
[41] T. Cordero-Lanzac, A. Ateka, P. Pérez-Uriarte, P. Castaño, A.T. Aguayo, J. Bilbao, Insight into the Deactivation and Regeneration of HZSM-5 Zeolite Catalysts in the Conversion of Dimethyl Ether to Olefins, Ind. Eng. Chem. Res 57 (2018) 13689–13702, https://doi.org/10.1021/acs.iecr.8b03308.
[42] P. Pérez-Uriarte, A. Ateka, M. Gamero, A.T. Aguayo, J. Bilbao, Effect of the Operating Conditions in the Transformation of DME to olefins over a HZSM-5 Zeolite Catalyst, Ind. Eng. Chem. Res 55 (2016) 6569–6578, https://doi.org/10.1021/acs.iecr.6b00627.
[43] P. Pérez-Uriarte, M. Gamero, A. Ateka, M. Díaz, A.T. Aguayo, J. Bilbao, Effect of the Acidity of HZSM-5 Zeolite and the Binder in the DME Transformation to Olefins, Ind. Eng. Chem. Res 55 (2016) 1513–1521, https://doi.org/10.1021/acs.iecr.5b04477.
[44] P. Pérez-Uriarte, A. Ateka, A.G. Gayubo, T. Cordero-Lanzac, A.T. Aguayo, J. Bilbao, Deactivation kinetics for the conversion of dimethyl ether to olefins over a HZSM-5 zeolite catalyst, Chem. Eng. J. 311 (2017) 367–377, https://doi.org/10.1016/j.cej.2016.11.104.
[45] Z. Chen, Z. Li, Y. Zhang, D. Chevella, G. Li, Y. Chen, X. Guo, J. Liu, J. Yu, A green route for the synthesis of nano-sized hierarchical ZSM-5 zeolite with excellent DTO catalytic performance, Chem. Eng. J. 388 (2020) 124322, https://doi.org/10.1016/j.cej.2020.124322.
[46] M.R. Sakha, P. Halimitabrizi, S. Soltanali, F. Ektefa, Z. Hajjar, D. Salari, Sustainable product-based approach in the production of olefins using a dual functional ZSM-5 catalyst, RSC Adv. 13 (2023) 7514–7523, https://doi.org/10.1039/D3RA00037K.
[47] F. Yaripour, Z. Shariatinia, S. Sahebdelfar, A. Irandoukht, Effect of boron incorporation on the structure, products selectivities and lifetime of H-ZSM-5 nanocatalyst designed for application in methanol-to-olefins (MTO) reaction, Microporous Mesoporous Mater. 203 (2015) 41–53, https://doi.org/10.1016/j.micromeso.2014.10.024.
[48] J.J. Kim, D.J. Jeong, H.S. Jung, Y.G. Hur, J.W. Choung, J.H. Baik, M.-J. Park, C.-H. Chung, J.W. Bae, Dimethyl ether conversion to hydrocarbons on the closely interconnected FER@ZSM-5 nanostructures, Microporous Mesoporous Mater. 340 (2022) 112034, https://doi.org/10.1016/j.micromeso.2022.112034.
[49] D. Romero, R. Rohling, L. Meng, M. Rigutto, E.J.M. Hensen, Shape selectivity in linear paraffins hydroconversion in 10-membered-ring pore zeolites, J. Catal. 394 (2021) 284–298, https://doi.org/10.1016/j.jcat.2020.11.007.
[50] L. Shirazi, E. Jamshidi, M.R. Ghasemi, The effect of Si/Al ratio of ZSM-5 zeolite on its morphology, acidity and crystal size, Cryst. Res. Technol. 43 (2008) 1300–1306, https://doi.org/10.1002/crat.200800149.
[51] W.O. Haag, R.M. Lago, P.G. Rodewald, Aromatics, light olefins and gasoline from methanol: Mechanistic pathways with ZSM-5 zeolite catalyst, J. Mol. Catal. 17 (1982) 161–169, https://doi.org/10.1016/0304-5102(82)85027-X.
[52] W. Khan, X. Jia, Z. Wu, J. Choi, A. Yip, Incorporating Hierarchy into Conventional Zeolites for Catalytic Biomass Conversions: A Review, Catalysts 9 (2019) 127, https://doi.org/10.3390/catal9020127.
[53] R. Srivastava, M. Choi, R. Ryoo, Mesoporous materials with zeolite framework: remarkable effect of the hierarchical structure for retardation of catalyst deactivation, Chem. Commun. (2006) 4489, https://doi.org/10.1039/b612116k.
[54] T. Weissenberger, B. Reiprich, A.G.F. Machoke, K. Klühspies, J. Bauer, R. Dotzel, J. L. Casci, W. Schwieger, Hierarchical MFI type zeolites with intracrystalline macropores: the effect of the macropore size on the deactivation behaviour in the MTO reaction, Catal. Sci. Technol. 9 (2019) 3259–3269, https://doi.org/10.1039/C9CY00368A.
[55] S. Mitchell, A.B. Pinar, J. Kenvin, P. Crivelli, J. Kärger, J. Pérez-Ramírez, Structural analysis of hierarchically organized zeolites, Nat. Commun. 6 (2015) 8633, https://doi.org/10.1038/ncomms9633.
[56] P. Losch, T. Hoff, J. Kolb, C. Bernardon, J.-P. Tessonnier, B. Louis, Mesoporous ZSM-5 Zeolites in Acid Catalysis: Top-Down vs. Bottom-Up Approach, Catalysts 7 (2017) 225, https://doi.org/10.3390/catal7080225.
[57] C. Liu, R. Zhang, R. Pei, C. Zhang, F. Li, Hierarchical ZSM-5 zeolite obtained by designed organosiloxane: synthesis, characterization, and catalytic applications, Can. J. Chem. 100 (2022) 568–574, https://doi.org/10.1139/cjc-2021-0252.
[58] E. Giglio, G. Ferrarelli, F. Salomone, E. Corrao, M. Migliori, S. Bensaid, R. Pirone, G. Giordano, Tailoring the acidity of ZSM-5 via surface passivation: Catalytic assessment on dimethyl ether to olefins (DTO) process, Fuel 362 (2024) 130559, https://doi.org/10.1016/j.fuel.2023.130559.
[59] E. Corrao, F. Salomone, E. Giglio, M. Castellino, S.M. Ronchetti, M. Armandi, R. Pirone, S. Bensaid, CO_2 conversion into hydrocarbons via modified Fischer-Tropsch synthesis by using bulk iron catalysts combined with zeolites, Chem. Eng. Res. Des. 197 (2023) 449–465, https://doi.org/10.1016/j.cherd.2023.07.052.
[60] C. Wen, J. Jiang, C. Chiliu, Z. Tian, X. Xu, J. Wu, C. Wang, L. Ma, Single-step selective conversion of carbon dioxide to aromatics over Na-Fe $_3$ O $_4$ /Hierarchical HZSM-5 zeolite catalyst, Energy Fuels 34 (2020) 11282–11289, https://doi.org/10.1021/acs.energyfuels.0c02120.
[61] Y.-P. Guo, H.-J. Wang, Y.-J. Guo, L.-H. Guo, L.-F. Chu, C.-X. Guo, Fabrication and characterization of hierarchical ZSM-5 zeolites by using organosilanes as additives, Chem. Eng. J. 166 (2011) 391–400, https://doi.org/10.1016/j.cej.2010.10.057.
[62] E. Catizzone, G. Ferrarelli, P. Bruno, G. Giordano, M. Migliori, Simultaneous catalytic dehydration of methanol and ethanol: How ZSM-5 acidity addresses conversion and products distribution, Catal. Today 427 (2024) 114436, https://doi.org/10.1016/j.cattod.2023.114436.
[63] Z. Qin, L. Lakiss, J.-P. Gilson, K. Thomas, J.-M. Goupil, C. Fernandez, V. Valtchev, Chemical equilibrium controlled etching of MFI-type zeolite and its influence on zeolite structure, acidity, and catalytic activity, Chem. Mater. 25 (2013) 2759–2766, https://doi.org/10.1021/cm400719z.
[64] I. Miletto, E. Catizzone, G. Bonura, C. Ivaldi, M. Migliori, E. Gianotti, L. Marchese, F. Frusteri, G. Giordano, In Situ FT-IR Characterization of CuZnZr/Ferrierite Hybrid Catalysts for One-Pot CO2-to-DME Conversion, Materials 11 (2018) 2275, https://doi.org/10.3390/ma11112275.
[65] A. Aloise, A. Marino, F. Dalena, G. Giorgianni, M. Migliori, L. Frusteri, C. Cannilla, G. Bonura, F. Frusteri, G. Giordano, Desilicated ZSM-5 zeolite: Catalytic performances assessment in methanol to DME dehydration, Microporous Mesoporous Mater. 302 (2020) 110198, https://doi.org/10.1016/j.micromeso.2020.110198.
[66] F. Salomone, E. Sartoretti, S. Ballauri, M. Castellino, C. Novara, F. Giorgis, R. Pirone, S. Bensaid, CO_2 hydrogenation to methanol over Zr- and Ce-doped indium oxide, Catal. Today 423 (2023) 114023, https://doi.org/10.1016/j.cattod.2023.01.030.
[67] M. Mezzapesa, F. Salomone, H. Guzmán, F. Zammillo, R. Millini, L. Bua, G. Marra, A. Tacca, R. Marrazzo, N. Russo, R. Pirone, S. Hernández, S. Bensaid, Development of In–Cu binary oxide catalysts for hydrogenating CO_2*via* thermocatalytic and electrocatalytic routes, Inorg. Chem. Front 11 (2024) 2319–2338, https://doi.org/10.1039/D3QI02499G.
[68] O. Levenspiel. Chemical Reaction Engineering, 3rd ed., John Wiley & Sons, Inc, 1998.
[69] K. Barbera, F. Bonino, S. Bordiga, T.V.W. Janssens, P. Beato, Structure–deactivation relationship for ZSM-5 catalysts governed by framework defects, J. Catal. 280 (2011) 196–205, https://doi.org/10.1016/j.jcat.2011.03.016.
[70] T.K. Phung, G. Busca, On the Lewis acidity of protonic zeolites, Appl. Catal. A Gen. 504 (2015) 151–157, https://doi.org/10.1016/j.apcata.2014.11.031.
[71] G.P. Babu, S.G. Hegde, S.B. Kulkarni, P. Ratnasamy, Active centres over HZSM5 zeolites:1. Xylene isomerization, J. Catal. 81 (1983) 471–477, https://doi.org/10.1016/0021-9517(83)90185-9.
[72] S. Bailleul, I. Yarulina, A.E.J. Hoffman, A. Dokania, E. Abou-Hamad, A. D. Chowdhury, G. Pieters, J. Hajek, K. De Wispelaere, M. Waroquier, J. Gascon, V. Van Speybroeck, A supramolecular view on the cooperative role of brønsted and lewis acid sites in zeolites for methanol conversion, J. Am. Chem. Soc. 141 (2019) 14823–14842, https://doi.org/10.1021/jacs.9b07484.